SCIENCE CHINA
Physics, Mechanics & Astronomy

• Article •

August 2017 Vol. 60 No. 8: 084612
doi: 10.1007/s11433-017-9037-3

XFEM modeling of hydraulic fracture in porous rocks with natural fractures

Tao Wang, ZhanLi Liu*, QingLei Zeng, Yue Gao, and Zhuo Zhuang*

Applied Mechanics Lab., School of Aerospace Engineering, Tsinghua University, Beijing 100084, China

Received January 12, 2017; accepted April 11, 2017; published online June 15, 2017

Hydraulic fracture (HF) in porous rocks is a complex multi-physics coupling process which involves fluid flow, diffusion and solid deformation. In this paper, the extended finite element method (XFEM) coupling with Biot theory is developed to study the HF in permeable rocks with natural fractures (NFs). In the recent XFEM based computational HF models, the fluid flow in fractures and interstitials of the porous media are mostly solved separately, which brings difficulties in dealing with complex fracture morphology. In our new model the fluid flow is solved in a unified framework by considering the fractures as a kind of special porous media and introducing Poiseuille-type flow inside them instead of Darcy-type flow. The most advantage is that it is very convenient to deal with fluid flow inside the complex fracture network, which is important in shale gas extraction. The weak formulation for the new coupled model is derived based on virtual work principle, which includes the XFEM formulation for multiple fractures and fractures intersection in porous media and finite element formulation for the unified fluid flow. Then the plane strain Kristianovic-Geertsma-de Klerk (KGD) model and the fluid flow inside the fracture network are simulated to validate the accuracy and applicability of this method. The numerical results show that large injection rate, low rock permeability and isotropic *in-situ* stresses tend to lead to a more uniform and productive fracture network.

hydraulic fracture, XFEM, porous media, fluid flow, multi-physics coupling

PACS number(s): 46.15.-x, 46.50.+a, 91.60.Ba

Citation: T. Wang, Z. L. Liu, Q. L. Zeng, Y. Gao, and Z. Zhuang, XFEM modeling of hydraulic fracture in porous rocks with natural fractures, Sci. China-Phys. Mech. Astron. **60**, 084612 (2017), doi: 10.1007/s11433-017-9037-3

1 Introduction

Hydraulic fracturing, also known as "fracking" [1], is the fracturing process of the formation driven by fluid overpressure, and is widely used in exploiting oil, gas and geothermal reservoirs. A successful fracking treatment may greatly increase the production of gas, which makes the technique economically attractive. Therefore, the optimization of the process related to fracking is becoming increasingly important.

Conventional modeling approaches to fracking problems are usually based on analytical 2D models, which were developed by assuming planar, symmetric, bi-wing crack geometries in infinite elastic medium, such as the Kristianovic-Geertsma-de Klerk (KGD) and Perkins-Kern-Nordgren (PKN) models [2,3]. For the KGD model, the fracture cross-section is assumed to have constant width. For the PKN model, the fracture cross-section is assumed to be elliptical and to maintain a constant height along the fracture. Later, planar three-dimensional (3D) and pseudo-three-dimensional (P3D) analytical or semi-analytical models are developed to obtain more complex fracture length, height, and width growth profiles [4]. These models provide valu-

*Corresponding authors (ZhanLi Liu, email: liuzhanli@tsinghua.edu.cn; Zhuo Zhuang, email: zhuangz@tsinghua.edu.cn)

able insight and perspectives for our understanding of the fracking problems and supply validation cases for comparison with numerical results.

Numerical simulation is an efficient way to improve the understanding of fracking and thus leads to better reservoir treatments. Many numerical methods have been proposed to model HF [5], such as displacement discontinuity method (DDM) [6], universal method [7], cohesive zone method (CZM) [8], discrete fracture network (DFN) method [9], phase field method [10] and extended finite element method (XFEM) [11,12]. The DDM is based on the boundary element method (BEM) [13] and requires to remesh the grid when the fracture propagates. It's easy to deal with the rock with faults, joints, fractures and other discontinuities. The universal method proposed by Hunsweck et al. [7] is a finite element method (FEM) based algorithm to simulate plane strain HF in an impermeable elastic media, and it can predict the existence of fluid lag [7]. The CZM is powerful in modeling adhesives, bonded interfaces and rock fractures [14], and it has been used to model HF [8,15]. The other applications of CZM for the analysis of HF include the work by Boone and Ingraffea [16], Mohammadnejad and Khoei [17], Carrier and Granet [18], Salehi and Nygaard [19]. The DFN method is based on analytical or semi-analytical solutions [9]. It has high efficiency in solving fracking problems and is widely used in commercial software in petroleum engineering. The phase field method can capture the fracture surface automatically and has attracted a sustained attention in the field of fracking recently [10,20].

For HF in petrol engineering, especially in shale gas extraction, the fluid flow in a porous rock has a major influence on the deformation and flow characteristics, so the rock has to be considered as porous media [5]. The simulation of fracking in porous media needs the modeling of (1) behavior of solid skeleton and fluid bulk phases, as well as their interaction; (2) fracture propagation in arbitrary paths; (3) fluid flow in the developed fracture network and porous medium. Nevertheless, most of the early HF models assume that the rock is impermeable, ignoring the interstitial flow in the media, but the interstitial flow is very important for understanding the complex fracture phenomenon in porous rocks. The fluid flow in a deformed porous media is first studied by Terzaghi [21] for one-dimensional (1D) consolidation problems. It has been extended to a 3D consolidation theory including Darcy's law of fluid transport by Biot [22]. Their pioneering work has attracted many researchers' interests due to its abundant practical applications. The fundamental mechanics applications for porous media have been illustrated by many researchers [23-25].

In the last decades, XFEM has emerged as a powerful numerical tool for the analysis of fracture problems [26-29] and recently has been widely used in solving complex HF problems by many researchers [30-34]. In the recent XFEM based computational HF models, the fluid flow in fractures and interstitials of the porous media are mostly solved separately. For the fluid transport in deforming porous media, the Darcy-Biot approach has been adopted as an extension of the standard materials [35,36]. For the fluid flow in the fracture, the classical Poiseuille law is often adopted for laminar flow of the incompressible viscous fluid [37]. Then by combining with a transport equation for fluid the pressure distribution along fracture surface can be obtained [16,38]. Gordeliy et al. [32] apply XFEM to solve the fully-coupled fracking problems. Gupta and Duarte [39] present the simulation of non-planar 3D HF, which focus on propagating fractures with complex geometries. The effect of Mode III stress intensity factors (SIFs) is also considered in the calculation of both fracture propagation direction and length. Faivre et al. [30] and Salimzadeh et al. [31] employ the XFEM models of the HF propagation in poroelasticity materials. Réthoré et al. [40] propose XFEM for incorporating discontinuity in the pressure field and use it in both unsaturated and saturated fracturing porous media. Recently, Khoei et al. [41,42] study the interaction between the HF and frictional natural fault using the XFEM technique. However, there still are some difficulties in dealing with the complex fluid flow in multi-fractures and fracture intersection in both 2D and 3D fracture networks [17,43-45]. For example, how to deal with the continuity of fluid flow and the distribution of fluid at the intersection of the fractures, the FEM formulation of the elements with two fractures. In this paper, the fluid flow in fractures and interstitials of the porous media are solved in a unified framework by regarding the fractures as the special porous media and introducing Poiseuille-type flow inside them. Multiple level sets are used to describe the fracture intersection, which is suitable for fracture network propagation along the arbitrary path. The most advantage of present method is that it is convenient to deal with fluid flow inside the multiple fractures and permeability of the rock. Based on this method, a fully coupled fracture network propagation problem is studied and some useful conclusions for engineering practice are given.

2 Coupling model and field equations

2.1 Problem description

Hydraulic fracture is a highly coupled problem between solid deformation and fluid flow, which contains the following aspects: (1) pore pressure in the media can cause expansion or contraction of solid, then deformation of solid can affect interstitial flow in the media; (2) fluid can drive fracture opening and propagating, then fracture opening in turn can affect the fluid flow in fracture; (3) the fluid will exchange between the fracture and the surrounding porous rocks. In order to simulate this highly coupled problem, some basic assumptions are introduced: (1) the media are permeable, elastic and brittle,

governed by the Biot constitutive relation and characterized by fracture toughness K_{IC}, Young's modulus E, Poisson's ratio ν, Biot constant α and undrained Poisson's ratio ν_u; (2) driving fluid is incompressible and has a constant dynamic viscosity μ; (3) fracture is a kind of special porous media and fluid flow inside the fracture is the Poiseuille-type flow; (4) fluid transport in the interstitial space can be described by the well-known Darcy's law; (5) gravity is neglected in the fluid transport equation.

The coupling method proposed is the combination of XFEM with Biot theory of poroelasticity, the fluid flow in the fracture and the interstitial flow in porous media are solved in a unified framework, multiple level set functions are used to describe multiple fractures and the intersection of the fractures, as shown in Figure 1.

2.2 Deformation of porous media

A general situation is considered here. The initial domain of a 3D deformation body is Ω_0 and the current domain is Ω. There are some discontinuous surfaces such as HFs and natural fractures denoted by Γ_c in Ω, as shown in Figure 2. The motion of a body can be described by $\boldsymbol{x}=\phi(\boldsymbol{X}, t)$, where $\boldsymbol{x}$ denotes spatial coordinate and $\boldsymbol{X}$ denotes material coordinate. The displacement field $\boldsymbol{u}$ can be written as:

$$\boldsymbol{u}=\boldsymbol{x}-\boldsymbol{X}=\phi(\boldsymbol{X},t)-\boldsymbol{X}. \tag{1}$$

A momentum equation in the updated Lagrangian description is

$$\nabla\cdot\boldsymbol{\sigma}+\rho\boldsymbol{b}-\rho\ddot{\boldsymbol{u}}=0, \quad \text{in} \quad \Omega, \tag{2}$$

where ∇ is material gradient, $\boldsymbol{\sigma}$ is Cauchy stress tensor, $\boldsymbol{b}$ is body force vector, ρ is an average mass density of the porous media defined as $\rho=(1-\varphi)\rho_s+\varphi\rho_w$, in which φ stands for the porosity of media, ρ_s and ρ_w are the densities of solid and fluid, respectively. The inertia effect is also considered by introducing the inertia item in momentum equation.

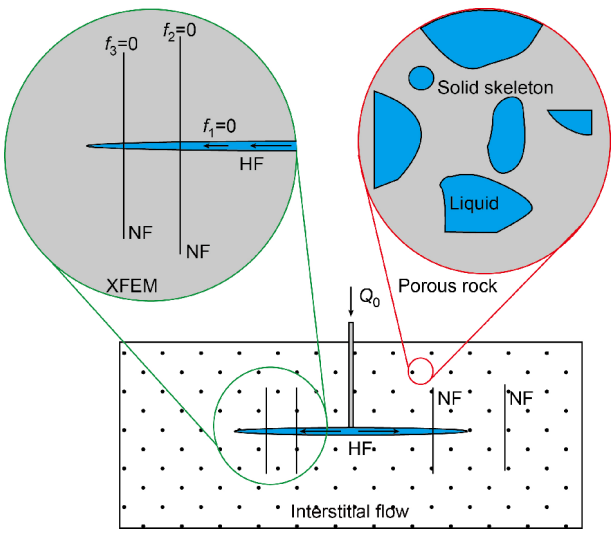

Figure 1 (Color online) Coupling framework for hydraulic fracture problem, f^i is the simplification of the signed distance function $f^i(\boldsymbol{X})$ to describe the location of the fracture.

The boundary Γ is a union set of displacement boundary (Γ_u), traction boundary (Γ_t) and crack surface (Γ_c). There are $\Gamma_u\cup\Gamma_t\cup\Gamma_c=\Gamma$ and $\Gamma_u\cap\Gamma_t=\varnothing$, as presented in Figure 2. Thus, the boundary conditions of porous solid are given by

$$\begin{aligned}&\boldsymbol{u}=\bar{\boldsymbol{u}}, \quad \text{on} \quad \Gamma_u,\\ &\boldsymbol{\sigma}\cdot\boldsymbol{n}=\bar{\boldsymbol{t}}, \quad \text{on} \quad \Gamma_t,\\ &\boldsymbol{\sigma}\cdot\boldsymbol{n}=\boldsymbol{t}_c, \quad \text{on} \quad \Gamma_c,\end{aligned} \tag{3}$$

where $\boldsymbol{n}$ is the normal direction to the related boundary, $\bar{\boldsymbol{u}}$ is the given displacement on Γ_u, $\bar{\boldsymbol{t}}$ is the given traction on Γ_t, and $\boldsymbol{t}_c$ is the traction on Γ_c. Note that the traction $\boldsymbol{t}_c$ imposed on HF and NF respectively represent fluid pressure P and contact traction $\boldsymbol{t}_{\text{cont}}$.

The fluid can affect the solids in two ways: (1) fracture opens and propagates under the fluid pressure, (2) expansion or contraction of the solid is caused by pore pressure. The first way is illustrated in details in sect. 4. For the second one, the Cauchy stress $\boldsymbol{\sigma}$ in an equilibrium equation is modified as the Biot effective stress $\boldsymbol{\sigma}'$:

$$\boldsymbol{\sigma}'=\boldsymbol{\sigma}+\alpha p\boldsymbol{I}, \tag{4}$$

where α is Biot coefficient, p is pore pressure and $\boldsymbol{I}$ is a second order identity tensor. Note that compressive stresses are negative.

2.3 Unified description of fluid flow in fracture and interstitial

2.3.1 Interstitial flow in porous media

The fluid flow in an interstitial space can be described by the proverbial Darcy's law, which is an empirical equation for interstitial flow in non-deformable porous media. It can also be derived from Navier-Stokes equations by discarding the inertial terms [46]. Neglecting the fluid density variation effect [47], Darcy's law can be employed as:

$$q_i=-\kappa\left(p_{,i}-b_{\text{fi}}\right), \tag{5}$$

where $\kappa=k/\mu$ is the permeability coefficient (k is intrinsic permeability, which has dimension of length squared, μ is fluid dynamic viscosity coefficient), $b_{\text{fi}}=\rho_{\text{f}}g_i$ is a body force per unit volume of fluid (ρ_{f} is fluid density, g_i is gravity component in i-direction).

Consideration of mass conservation of a compressible fluid leads to the local continuity equation:

$$\frac{\partial\zeta}{\partial t}+q_{i,i}=\gamma, \tag{6}$$

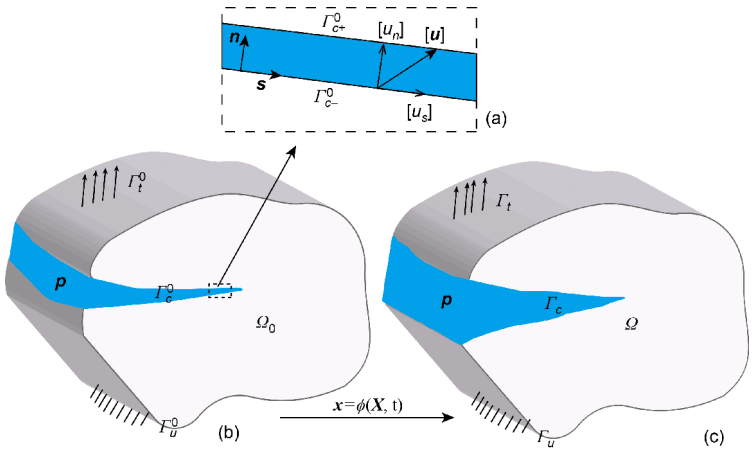

Figure 2 (Color online) Hydraulic driving fracture. (a) Orientation of normal and tangent vectors of local fracture surface, and the displacement jump vector; the 3D body with hydro-discontinuity represented by initial configuration (b) and current configuration (c).

where γ is flux source density (i.e. a rate of injected fluid volume per unit volume of the porous media). Note that eq. (6) is in a linearized form since the variation effect of fluid density is neglected, such that the fluid is incompressible.

The boundary of fluid flow Γ is a union set of the prescribed pressure boundary (Γ_p) and flow boundary (Γ_q). The boundary conditions are given by

$$\begin{aligned} &\kappa \nabla p = \overline{\boldsymbol{q}}, \quad \text{on} \quad \Gamma_q, \\ &p = \overline{p}, \quad \text{on} \quad \Gamma_p, \end{aligned} \tag{7}$$

where $\overline{\boldsymbol{q}}$ is the given volume flux on Γ_q and $\overline{p}$ is the given pressure on Γ_p. There are $\Gamma_q \cup \Gamma_p = \Gamma$ and $\Gamma_q \cap \Gamma_p = \varnothing$.

For the fluid filled porous media, the Biot formulation of constitutive equations is based on the assumptions of linearity between stress (σ_{ij}, p) and strain $(\varepsilon_{ij}, \zeta)$. It is reversibility of the deformation process, which means that there is no energy dissipation during a closed loading cycle. With the respective addition of scalar pore pressure p and variation of fluid content ζ to stress and strain group, the Biot linear constitutive relations can be obtained by extending the known elastic expressions. Particularly, the most general form of an isotropic poroelasticity material response is

$$\sigma_{ij} + \alpha p \delta_{ij} = 2G\varepsilon_{ij} + \frac{2G\nu}{1-2\nu}\varepsilon_v \delta_{ij}, \tag{8}$$

$$p = M(\zeta - \alpha \varepsilon_v). \tag{9}$$

Without the pore pressure p, eq. (8) degenerates to the classical elastic constitutive relation. The parameters G and ν are thus identified as the shear modulus and Poisson's ratio of the drained elastic solid. The additional Biot constitutive constants α and M characterize the relation of stress and strain coupling between solid and fluid. Biot modulus M can be expressed:

$$M = \frac{2G(\nu_u - \nu)}{\alpha^2(1-2\nu_u)(1-2\nu)}, \tag{10}$$

where ν_u is Poisson's ratio of the undrained elastic solid.

Combination of Darcy's law eq. (5), continuity eq. (6), and constitutive relation eqs. (8) and (9) leads to the governing equation of pore pressure p [24]:

$$\frac{\partial p}{\partial t} - \nabla \cdot (\kappa M \nabla p) = -\alpha M \frac{\partial u_{i,i}}{\partial t} + M(\gamma - \kappa b_{\mathrm{fi},i}). \tag{11}$$

Thus, the diffusion of pore pressure is coupled with the change rate of volumetric strain. In a steady state, eq. (11) is uncoupled and becomes a Poisson equation; while in a dynamic situation, the pressure field is coupled with the deformation field.

It is interesting to note that the diffusivity coefficient for pore pressure equation can be expressed as a ratio of mobility coefficient κ to a storage coefficient $1/M$. The storage coefficient is defined under the constraint of zero volumetric strain for pore pressure.

2.3.2 *Fluid flow in fracture*

The fracture is also regarded as a kind of porous media considering the permeability coefficient $\kappa = k/\mu$. However, a modification of fluid transport is needed to account for an increase of fluid flow inside the opening fracture. On the phenomenological level and at a range of fracture opening where Navier-Stokes free flow is not explicitly considered, this can be simulated by a modification of Darcy's law by adding an additional part $\kappa_{\mathrm{frac}} = w^2/12\mu$ to the fluid flux along tangential direction of fracture. Thus, the mobility coefficient κ at each point in the whole domain is expressed as:

$$\kappa = \begin{cases} w^2/12\mu, & \text{in tangential of fracture,} \\ k/\mu, & \text{otherwise.} \end{cases} \tag{12}$$

The constitutive modeling of the additional part κ_{frac} should account for a Poiseuille-type flow, governed by the above quadratic dependence on the fracture opening w which is visualized in Figure 2(a).

The fracture is a curved surface where the mobility coefficient κ varies in different directions. There are two directions tangential to facture surface and one direction perpendicular to the surface. In a local fracture surface coordinate system, a mobility coefficient matrix is defined:

$$\boldsymbol{\kappa}_{\text{local}} = \text{diag}\left(\frac{w^2}{12\mu}, \frac{w^2}{12\mu}, \frac{k}{\mu}\right). \tag{13}$$

3 Weak form of coupling equation

The discrete equations are constructed by the standard Galerkin procedures. The admissible space for the displacement and pressure fields is defined as follows:

$$U = \left\{ \begin{array}{l} \boldsymbol{u}(\boldsymbol{X},t) \,\middle|\, \boldsymbol{u}(\boldsymbol{X},t) \in C^0, \boldsymbol{u}(\boldsymbol{X},t) = \bar{\boldsymbol{u}}(t), \text{ on}\Gamma_{\text{u}}, \boldsymbol{u} \text{ discontinuous on}\Gamma_{\text{c}}, \\ p(\boldsymbol{X},t) \,\middle|\, p(\boldsymbol{X},t) \in C^0, p(\boldsymbol{X},t) = \bar{p}(t), \text{ on}\Gamma_p, \end{array} \right\} \tag{14}$$

$$U_0 = \left\{ \begin{array}{l} \delta\boldsymbol{u}(\boldsymbol{X},t) \,\middle|\, \delta\boldsymbol{u}(\boldsymbol{X},t) \in C^0, \delta\boldsymbol{u}(X,t) = 0, \text{on}\Gamma_{\text{u}}, \delta\boldsymbol{u} \text{ discontinuous on}\Gamma_{\text{c}}, \\ \delta p(\boldsymbol{X},t) \,\middle|\, \delta p(\boldsymbol{X},t) \in C^0, \delta p(\boldsymbol{X},t) = 0, \text{ on}\Gamma_p. \end{array} \right\} \tag{15}$$

The weak form of momentum equation is given by for $\boldsymbol{u}(\boldsymbol{X},t) \in U$.

$$\begin{aligned} &\delta W^{\text{kin}} = \delta W^{\text{ext}} - \delta W^{\text{int}} - \delta W^{\text{pore}} - \delta W^{\text{c}} \\ &\forall \delta\boldsymbol{u}(\boldsymbol{X}) \in U_0, \end{aligned} \tag{16}$$

where δW^{kin} is virtual kinetic work performed by inertia, δW^{ext} is virtual external work performed by applied loads, δW^{int} is virtual internal work, δW^{pore} is virtual work performed by pore pressure, δW^{c} is virtual work performed by fluid pressure or contact traction on the HF and NF surface Γ_{c}.They are respectively defined by

$$\delta W^{\text{kin}} = \int_{\Omega\setminus\Gamma_{\text{c}}} \delta\boldsymbol{u} \cdot \rho\ddot{\boldsymbol{u}} \text{d}\Omega, \tag{17}$$

$$\delta W^{\text{ext}} = \int_{\Omega\setminus\Gamma_{\text{c}}} \delta\boldsymbol{u} \cdot \rho\boldsymbol{b} \text{d}\Omega + \int_{\Gamma_{\text{t}}} \delta\boldsymbol{u} \cdot \bar{\boldsymbol{t}}\, \text{d}\Gamma, \tag{18}$$

$$\delta W^{\text{int}} = \int_{\Omega\setminus\Gamma_{\text{c}}} \frac{\partial\delta\boldsymbol{u}}{\partial\boldsymbol{x}} \cdot \boldsymbol{\sigma} \text{d}\Omega, \tag{19}$$

$$\delta W^{\text{pore}} = \int_{\Omega\setminus\Gamma_{\text{c}}} \delta\boldsymbol{u} \cdot \alpha \frac{\partial p}{\partial\boldsymbol{x}} \text{d}\Omega, \tag{20}$$

$$\delta W^{\text{c}} = \int_{\Gamma_{\text{c}}} \delta\boldsymbol{u} \cdot \boldsymbol{t}_{\text{c}} \text{d}\Gamma. \tag{21}$$

Substituting eqs. (17)-(21) into the momentum eq. (16), the weak form of momentum equation can be given by

$$\begin{aligned} &\int_{\Omega\setminus\Gamma_{\text{c}}} \delta\boldsymbol{u} \cdot \rho\ddot{\boldsymbol{u}} \text{d}\Omega \\ &= \int_{\Omega\setminus\Gamma_{\text{c}}} \delta\boldsymbol{u} \cdot \rho\boldsymbol{b} \text{d}\Omega + \int_{\Gamma_{\text{t}}} \delta\boldsymbol{u} \cdot \bar{\boldsymbol{t}}\, \text{d}\Gamma - \int_{\Omega\setminus\Gamma_{\text{c}}} \frac{\partial\delta\boldsymbol{u}}{\partial\boldsymbol{x}} \cdot \boldsymbol{\sigma} \text{d}\Omega \\ &\quad - \int_{\Omega\setminus\Gamma_{\text{c}}} \delta\boldsymbol{u} \cdot \alpha \frac{\partial p}{\partial\boldsymbol{x}} \text{d}\Omega - \int_{\Gamma_{\text{c}}} \delta\boldsymbol{u} \cdot \boldsymbol{t}_{\text{c}} \text{d}\Gamma. \end{aligned} \tag{22}$$

Using Galerkin weighting, the variation form of diffusion eq. (11) can be obtained by multiplying any kinematically admissible test function for the fluid pressure δp:

$$\Pi(p) = \int_{\Omega} \delta p \cdot \left\{ \frac{\partial p}{\partial t} - \nabla \cdot (\kappa M \nabla p) + \alpha M \frac{\partial u_{i,i}}{\partial t} - M\gamma + \kappa M b_{\text{fi},i} \right\} \text{d}\Omega. \tag{23}$$

Adopting the standard Galerkin procedure, the weak form of pressure field equation can be obtained by applying the divergence theorem, imposing the natural boundary conditions and satisfying the prescribed pressure boundary conditions:

$$\int_{\Omega} \nabla(\delta p) \cdot (\kappa M \nabla p) \text{d}\Omega + \int_{\Omega} \delta p \cdot \alpha M \nabla \cdot \dot{\boldsymbol{u}} \text{d}\Omega + \int_{\Omega} \delta p \cdot \dot{p}\, \text{d}\Omega = \int_{\Gamma_q} \delta p \cdot \kappa M \frac{\partial p}{\partial\boldsymbol{x}} \cdot \boldsymbol{n} \text{d}\Gamma + \int_{\Omega} \delta p \cdot M\gamma \text{d}\Omega + \int_{\Omega} \nabla(\delta p) \cdot (\kappa M \boldsymbol{b}_{\text{f}}) \text{d}\Omega. \tag{24}$$

4 XFEM discretization

4.1 Approximation of displacement and pressure field

Each fracture surface is implicitly described by the signed distance function $f^i(\boldsymbol{X})$, so that $f^i(\boldsymbol{X})$=0 indicates fracture surface, which can be dispersed in terms of shape function $N(\boldsymbol{X})$:

$$\sum_I N_I(\boldsymbol{X}) f_I^i = 0. \tag{25}$$

A fracture tip position function $g^i(\boldsymbol{X}, t)$ is also defined so that the fracture is contained within the sub-domain $g^i(\boldsymbol{X}, t)$>0.

Thus, the fracture surface is defined by

$$\boldsymbol{X} \in \Gamma_c^0 \quad \text{if} \quad f^i(\boldsymbol{X}) = 0 \quad \text{and} \quad g^i(\boldsymbol{X}, t) > 0. \tag{26}$$

Note that the implicit functions $f^i(\boldsymbol{X})$ and $g^i(\boldsymbol{X}, t)$ are only needed to be defined locally around the fracture. Furthermore, for elementwise propagation of the fracture, the function $g^i(\boldsymbol{X}, t)$ can be replaced by the index set of those fractured elements.

The conventional XFEM displacement field is expressed by [48]:

$$\boldsymbol{u}(\boldsymbol{X}, t) = \sum_{I=1}^{n_e} N_I(\boldsymbol{X}) \cdot \left\{ \boldsymbol{u}_I(t) + \sum_{i=1}^{n_F} \boldsymbol{q}_I^i \left[H(f^i(\boldsymbol{X})) - H\left(f^i(\boldsymbol{X}_I)\right) \right] \right\}, \tag{27}$$

where n_e is the number of nodes in the element, n_F is the number of fractures, including HF and NF, $\boldsymbol{u}_I(t)$ is the displacement of node I, $\boldsymbol{q}_I^i(t)$ is the additional freedom of node I for i-th fracture, and $H(x)$ is a Heaviside function:

$$H(x) = \begin{cases} 1 & x > 0, \\ 0 & x \le 0. \end{cases} \tag{28}$$

Expanding eq. (27) and subdividing each term into parts which are associated with $f^i(\boldsymbol{X})<0$ and $f^i(\boldsymbol{X})>0$, we have

$$\boldsymbol{u} = \sum_{i=q}^{n_F} \sum_{I=1}^{n_e} \boldsymbol{u}_I N_I (1 - H^i) + \boldsymbol{u}_I N_I H^i + \boldsymbol{q}_I \left(H^i - H_I^i\right) N_I, \tag{29}$$

where $H^i = H(f^i(\boldsymbol{X}))$, $H_I^i = H\left(f^i(\boldsymbol{X}_I)\right)$ and $N_I = N_I(\boldsymbol{X})$ for simplification.

By a rearrangement of the extended finite element basis and the nodal degrees of freedom, the fracture can be represented by superposed elements and phantom nodes. Thus, for elements with only one fracture, the displacement field of eq. (29) can be rewritten as:

$$\boldsymbol{u}(\boldsymbol{X}, t) = \sum_{I \in S_1} \boldsymbol{u}_I^1(t) N_I(\boldsymbol{X}) H(-f^1(\boldsymbol{X})) + \sum_{I \in S_2} \boldsymbol{u}_I^2(t) N_I(\boldsymbol{X}) H(f^1(\boldsymbol{X})). \tag{30}$$

For elements containing two cross-fractures, the displacement field of eq. (29) can be rewritten as:

$$\begin{aligned} \boldsymbol{u}(\boldsymbol{X}, t) = & \sum_{I \in S_1} \boldsymbol{u}_I^1(t) N_I(\boldsymbol{X}) H(-f^1(\boldsymbol{X})) H(-f^2(\boldsymbol{X})) + \sum_{I \in S_2} \boldsymbol{u}_I^2(t) N_I(\boldsymbol{X}) H(-f^1(\boldsymbol{X})) H(f^2(\boldsymbol{X})) \\ & + \sum_{I \in S_3} \boldsymbol{u}_I^3(t) N_I(\boldsymbol{X}) H(f^1(\boldsymbol{X})) H(-f^2(\boldsymbol{X})) + \sum_{I \in S_4} \boldsymbol{u}_I^4(t) N_I(\boldsymbol{X}) H(f^1(\boldsymbol{X})) H(f^2(\boldsymbol{X})), \end{aligned} \tag{31}$$

where S_i is the node sets of superposed element I, $\boldsymbol{u}_I^i$ is the nodal degrees of freedom of the superposed element i, and defined as:

$$\boldsymbol{u}_I^i = \boldsymbol{u}_I + \sum_{i=1}^{n_F} \boldsymbol{q}_I^i H\left(f^i(\boldsymbol{X}_I)\right). \tag{32}$$

Each element contains both the original real nodes and phantom nodes. Such recasting simplifies the implementation of XFEM effectively, since the nodal force of superposed elements can be calculated in the same way as in the conventional FEM [49].

The fracture is embodied by the presence of a displacement jump $[\boldsymbol{u}]=\boldsymbol{u}^+-\boldsymbol{u}^-$ across Γ_c, with $\boldsymbol{u}^+$ and $\boldsymbol{u}^-$ denoting the displacement along Γ_c^+ and Γ_c^-, respectively.

The normal and shear displacement jump $w = [\![u_n]\!]$ and $v = [\![u_{t_1}]\!]$ along Γ_c are defined as:

$$w = [\![\boldsymbol{u}]\!] \cdot \boldsymbol{n}, \quad v = [\![\boldsymbol{u}]\!] \cdot \boldsymbol{t}_1, \tag{33}$$

where w and v will be referred to as the "aperture" and "ride", respectively.

In order to discretize the diffusion eq. (11), the suitable shape function expression is taken for the pressure field in both fracture and rocks. Since the fracture does not impose any discontinuity in the fluid flow, the fluid pressure as well as the pore pressure should not be enriched to ensure the fluid flow continuity across the fracture, and they are approximated using the standard FEM as [50]:

$$p(\boldsymbol{X}, t) = \sum_I N_I(\boldsymbol{X}) p_I(t), \tag{34}$$

where p_I is the pore pressure at node I or the fluid pressure in the fracture located at the phantom node I.

4.2 Discretization of equilibrium and flow equations

By performing the spatial discretization of eq. (22), the discrete momentum equation of the solid is expressed as:

$$\boldsymbol{M}\ddot{\boldsymbol{u}} = \boldsymbol{f}^{\text{ext}} - \boldsymbol{f}^{\text{int}} - \boldsymbol{f}^{\text{pore}} - \boldsymbol{f}^{\text{fluid}} - \boldsymbol{f}^{\text{cont}}, \tag{35}$$

where $\boldsymbol{M}$ is mass matrix, $\boldsymbol{f}^{\text{ext}}$, $\boldsymbol{f}^{\text{int}}$, $\boldsymbol{f}^{\text{pore}}$, $\boldsymbol{f}^{\text{fluid}}$ and $\boldsymbol{f}^{\text{cont}}$ are the nodal external force, internal force, pore pressure force, fracture fluid force and contact traction force, respectively. They are assembled from each element node. Please note that bold $\boldsymbol{f}$ is nodal force, f is level set value; and bold $\boldsymbol{M}$ is mass matrix, M is Biot modulus.

For a fractured element e that is divided into two elements, its two superposed elements nodal forces can be written as:

$$\boldsymbol{M}_{ei} = \int_{\Omega^e} \rho \boldsymbol{N}^{\mathrm{T}} \boldsymbol{N} H((-1)^{i+1} f^e(\boldsymbol{X})) \mathrm{d}\Omega, \tag{36}$$

$$\begin{aligned} \boldsymbol{f}_{ei}^{\mathrm{ext}} &= \int_{\Omega^e} \rho \boldsymbol{N}^{\mathrm{T}} \boldsymbol{b} H((-1)^{i+1} f^e(\boldsymbol{X})) \mathrm{d}\Omega \\ &\quad + \int_{\Gamma_{\mathrm{t}}^e} \boldsymbol{N}^{\mathrm{T}} \bar{\boldsymbol{t}} H((-1)^{i+1} f^e(\boldsymbol{X})) \mathrm{d}\Gamma, \end{aligned} \tag{37}$$

$$\boldsymbol{f}_{ei}^{\mathrm{int}} = \int_{\Omega^e} \boldsymbol{B}^{\mathrm{T}} \boldsymbol{\sigma}_e H((-1)^{i+1} f^e(\boldsymbol{X})) \mathrm{d}\Omega, \tag{38}$$

$$\boldsymbol{f}_{ei}^{\mathrm{pore}} = \int_{\Omega^e} \alpha \boldsymbol{N}^{\mathrm{T}} \frac{\partial p}{\partial \boldsymbol{x}} H((-1)^{i+1} f^e(\boldsymbol{X})) \mathrm{d}\Omega, \tag{39}$$

$$\boldsymbol{f}_{ei}^{\mathrm{fluid}} = (-1)^i \int_{\Gamma_{\mathrm{c}}^e} \boldsymbol{N}^{\mathrm{T}} p \boldsymbol{n} \mathrm{d}\Gamma, \tag{40}$$

$$\boldsymbol{f}_{ei}^{\mathrm{cont}} = (-1)^i \int_{\Gamma_{\mathrm{c}}^e} \boldsymbol{N}^{\mathrm{T}} \boldsymbol{t}_{\mathrm{c}} \mathrm{d}\Gamma, \tag{41}$$

where i denotes the superposed elements, as shown in Figure 3. $\boldsymbol{B}$ is the discrete strain-displacement operator matrix with respect to the current coordinates [51]. The expression is similar for a case where an element is divided into four superposed elements. Note that the nodal force vector $\boldsymbol{f}_e$ is a sum of the nodal forces from two superposed elements, i.e.

$$\boldsymbol{f}_e = \sum_{i=1}^{2^{n_{\mathrm{F}}}} \boldsymbol{f}_{ei}, \tag{42}$$

where $\boldsymbol{f}_{ei}$ is the force vectors of the superposed element i.

Substituting eq. (34) into eq. (26) and neglecting the body force of fluid, the discrete form of the coupled seepage eq. (11) can be derived:

$$\boldsymbol{C}\dot{p} = \boldsymbol{P} - \boldsymbol{K}p - \boldsymbol{H}\dot{\boldsymbol{u}}, \tag{43}$$

where

$$\boldsymbol{C} = \int_{\Omega} \boldsymbol{N}^{\mathrm{T}} \frac{1}{M} \boldsymbol{N} \mathrm{d}\Omega, \tag{44}$$

$$\boldsymbol{K} = \int_{\Omega} (\nabla \boldsymbol{N})^{\mathrm{T}} \cdot \mathrm{diag}\left(\frac{w^2}{12\mu}, \frac{w^2}{12\mu}, \frac{k}{\mu} \right) \cdot \nabla \boldsymbol{N} \mathrm{d}\Omega, \tag{45}$$

$$\boldsymbol{H} = \int_{\Omega} (\nabla \boldsymbol{N})^{\mathrm{T}} \cdot \alpha \boldsymbol{N} \mathrm{d}\Omega, \tag{46}$$

$$\boldsymbol{P} = \int_{\Omega} \gamma \boldsymbol{N} \mathrm{d}\Omega + \int_{\Gamma_q} (\bar{\boldsymbol{q}} \cdot \boldsymbol{n}) \boldsymbol{N} \mathrm{d}\Gamma, \tag{47}$$

where $\boldsymbol{N}$ is shape function matrix and $\bar{\boldsymbol{q}}$ is the given fluid flux on prescribed flow boundary.

In summary, the finial discretization equation of the coupled problem is the combination of eqs. (35) and (43).

5 Numerical strategy

5.1 Integration scheme

For evaluation of the integrals eqs. (36)-(42) in the elements in which a Heaviside function appears, a modified numerical quadrature method such as subdomain integration should be adopted [52]. The element is divided into several subdomains, and each subdomain is integrated individually. However, some difficulties arise in subdomain integration method when the propagating fracture is considered. For example, if the fracture cuts the element into a very small domain, the accurate integration in this small domain requests a large number of integral points in the element, which results in lower efficiency. To suppress the need for element subdivision, Natarajan et al. [53-55] use a simple integration method proposed for polygonal domains, which is accurate and less sensitive to mesh distortion. In this paper, one-point integration method is adopted to improve the efficiency. The hourglass control is used in the element. More details on the hourglass control scheme are illustrated in refs. [56,57]. Using one-point integration, it is naturally assumed that the stresses are constant within the element and given by the values at the origin of parent coordinate system.

Expanding eqs. (36)-(42) with one-point integration, each item in the discrete momentum eq. (35) can be expressed as:

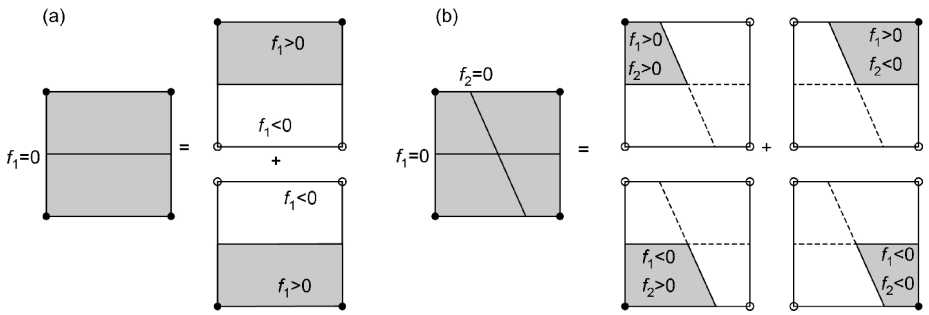

Figure 3 Decomposition of a fractured element into two elements (a), four elements (b): solid and hollow circles denote the original nodes and additional phantom nodes, respectively.

$$\boldsymbol{M}_{(e1/e2)} = \frac{V_{(e1/e2)}}{V}\int_{\Omega^e}\rho\boldsymbol{N}^{\mathrm{T}}\boldsymbol{N}\,\mathrm{d}\Omega, \tag{48}$$

$$\boldsymbol{f}_{e1}^{\ \mathrm{ext}} = \frac{V_{e1}}{V}\int_{\Omega^e}\rho\boldsymbol{N}^{\mathrm{T}}\boldsymbol{b}\,\mathrm{d}\Omega + \int_{\Gamma_{\mathrm{t}}^e}\boldsymbol{N}^{\mathrm{T}}\bar{\boldsymbol{t}}H(f^e(\boldsymbol{X}))\mathrm{d}\Gamma, \tag{49}$$

$$\boldsymbol{f}_{e2}^{\ \mathrm{ext}} = \frac{V_{e2}}{V}\int_{\Omega^e}\rho\boldsymbol{N}^{\mathrm{T}}\boldsymbol{b}\,\mathrm{d}\Omega + \int_{\Gamma_{\mathrm{t}}^e}\boldsymbol{N}^{\mathrm{T}}\bar{\boldsymbol{t}}H(-f^e(\boldsymbol{X}))\mathrm{d}\Gamma, \tag{50}$$

$$\boldsymbol{f}_{(e1/e2)}^{\ \mathrm{int}} = \frac{V_{(e1/e2)}}{V}\int_{\Omega^e}\left\{\boldsymbol{B}^{\mathrm{T}}\boldsymbol{\sigma}_{(e1/e2)} + \boldsymbol{f}_{(e1/e2)}^{\ \mathrm{stab}}\right\}\mathrm{d}\Omega, \tag{51}$$

$$\boldsymbol{f}_{(e1/e2)}^{\ \mathrm{pore}} = \frac{V_{(e1/e2)}}{V}\int_{\Omega^e}\alpha\boldsymbol{N}^{\mathrm{T}}\frac{\partial p}{\partial \boldsymbol{x}}\mathrm{d}\Omega, \tag{52}$$

$$\boldsymbol{f}_{(e1/e2)}^{\ \mathrm{fluid}} = -p\cdot A_{\Gamma_e^{\mathrm{c}}}\boldsymbol{n}_{(e1/e2)}, \tag{53}$$

$$\boldsymbol{f}_{ei}^{\ \mathrm{cont}} = (-1)^i\int_{\Gamma_{\mathrm{c}}^e}\boldsymbol{N}^{\mathrm{T}}\boldsymbol{t}_{\mathrm{c}}\mathrm{d}\Gamma, \tag{54}$$

where V is the total volume of the unfractured element, V_{ei} is the activated volume (the region surrounded by solid line in Figure 3) of the corresponding superposed element which consists of regular and phantom nodes. $\boldsymbol{f}^{\mathrm{stab}}$ in eq. (51) is a stabilization force vector to control hourglass modes since the one-point integration scheme is adopted [56]. $A_{\Gamma_e^{\mathrm{c}}}$ is the fracture surface area generated by cutting the element e with fracture surface, and $\boldsymbol{n}_{(e1/e2)}$ is normal vector of each fracture surface in the elements, note that $\boldsymbol{n}_{e1}=-\boldsymbol{n}_{e2}$.

As shown in eqs. (48)-(53), during calculating the force vectors for a fractured element, we can only modify them by the element volume fraction. This modification can be easily implemented into the standard FEM process, which is an extraordinary merit of the phantom node method in comparison with the conventional XFEM.

5.2 Explicit time integration

The explicit time integration is used for both solid fracture and fluid flow over a whole domain. The dynamics analysis procedure is based upon the implementation of an explicit integration rule together with the use of lumped mass matrices. The momentum eq. (35) is integrated using the central-difference integration rule, which can be expressed as:

$$\begin{aligned}\dot{\boldsymbol{u}}^{(i+1/2)} &= \dot{\boldsymbol{u}}^{(i-1/2)} + \frac{\Delta t_{(i+1)}+\Delta t_{(i)}}{2}\ddot{\boldsymbol{u}}^{(i)},\\ \boldsymbol{u}^{(i+1)} &= \boldsymbol{u}^{(i)} + \Delta t_{(i+1)}\dot{\boldsymbol{u}}^{(i+1/2)},\end{aligned} \tag{55}$$

where $\dot{\boldsymbol{u}}$ is velocity vector and $\ddot{\boldsymbol{u}}$ is acceleration vector, the subscript i refers to the increment number in an explicit time step. The central-difference integration is explicit in the sense that the kinematic state is advanced using the known values of $\dot{\boldsymbol{u}}^{(i-1/2)}$ and $\ddot{\boldsymbol{u}}^{(i)}$ from the previous increment.

The coupled seepage eq. (43) is integrated using the explicit forward-difference time integration rule, which can be given as:

$$p^{(i+1)} = p^{(i)} + \Delta t_{(i+1)}\dot{p}^{(i)}. \tag{56}$$

The key to improving the computational efficiency is to use the lumped mass matrix $\boldsymbol{M}$ and lumped capacitance matrix $\boldsymbol{C}$.

$$\ddot{\boldsymbol{u}}^{(i)} = \boldsymbol{M}^{-1}\cdot\left(\boldsymbol{F}^{(i)} - \boldsymbol{F}_I^{(i)}\right), \tag{57}$$

$$\dot{p}^{(i)} = \boldsymbol{C}^{-1}\cdot\left(\boldsymbol{P}^{(i)} - \boldsymbol{P}_q^{(i)}\right), \tag{58}$$

where $\boldsymbol{F}$ is the applied load vector, $\boldsymbol{F}_I$ is the internal force vector, $\boldsymbol{P}$ is the applied nodal source vector, and $\boldsymbol{P}_I$ is the internal flux vector.

5.3 Fracture propagation criterion

The stress and displacement fields at fracture tip are the essential to establish fracture criteria. We consider the general mixed-mode fractures with two modes as mode I and II. In terms of the polar coordinate (r, θ) centered at the fracture front, where r is the distance from the fracture front, and θ is the counterclockwise angle relative to the tangent to fracture surface at the front location, the stress components of fracture tip stress field in polar coordinate is written as [58]:

$$\begin{aligned}\sigma_{rr} &= \frac{1}{\sqrt{2\pi r}}\left[\frac{K_{\mathrm{I}}}{4}\left(5\cos\frac{\theta}{2}-\cos\frac{3\theta}{2}\right)+\frac{K_{\mathrm{II}}}{4}\left(-5\sin\frac{\theta}{2}+3\sin\frac{3\theta}{2}\right)\right],\\ \sigma_{\theta\theta} &= \frac{1}{\sqrt{2\pi r}}\left[\frac{K_{\mathrm{I}}}{4}\left(3\cos\frac{\theta}{2}+\cos\frac{3\theta}{2}\right)+\frac{K_{\mathrm{II}}}{4}\left(-3\sin\frac{\theta}{2}-3\sin\frac{3\theta}{2}\right)\right],\\ \sigma_{r\theta} &= \frac{1}{\sqrt{2\pi r}}\left[\frac{K_{\mathrm{I}}}{4}\left(\sin\frac{\theta}{2}+\sin\frac{3\theta}{2}\right)+\frac{K_{\mathrm{II}}}{4}\left(\cos\frac{\theta}{2}+3\cos\frac{3\theta}{2}\right)\right],\end{aligned} \tag{59}$$

where K_{I} and K_{II} are the stress intensity factors (SIFs) of modes I and II, respectively.

In the fracture criterion adopted, it's assumed that fracture propagates when the circumferential stress reaches the critical value, which is related to the fracture toughness [59], at the crack tip location in terms of polar coordinate (r, θ). In accordance with linear elastic fracture mechanics (LEFM), this criterion can be extended to the fractured orthotropic materials for plane problems [60,61]. The criterion can be expressed as:

$$\begin{aligned}&\left.\frac{\partial\sigma_{\theta\theta}}{\partial\theta}\right|_{\theta=\theta_{\mathrm{c}}} = 0, \quad \left.\frac{\partial^2\sigma_{\theta\theta}}{\partial\theta^2}\right|_{\theta=\theta_{\mathrm{c}}} < 0,\\ &\sigma_{\theta\theta\max} = \sigma_{\theta\theta}\Big|_{\theta=\theta_{\mathrm{c}}} = \frac{K_{\theta\max}}{\sqrt{2\pi r}}, K_{\theta\max} = K_{IC}.\end{aligned} \tag{60}$$

By substituting the stress component $\sigma_{\theta\theta}$ of eq. (59) into eq. (60), the fracture criterion for homogenous material is given by

$$K_{\mathrm{I}}\sin\theta_{\mathrm{c}}+K_{\mathrm{II}}(3\cos\theta_{c}-1)=0, \tag{61}$$

$$\frac{1}{4}\left[K_{\mathrm{I}}\left(3\cos\frac{\theta_{\mathrm{c}}}{2}+\cos\frac{3\theta_{\mathrm{c}}}{2}\right)-3K_{\mathrm{II}}\left(\sin\frac{\theta_{\mathrm{c}}}{2}+\sin\frac{3\theta_{\mathrm{c}}}{2}\right)\right]=K_{IC}. \tag{62}$$

The above equations can be solved by

$$\theta_{\mathrm{c}}=2\tan^{-1}\frac{1}{4}\left(\frac{K_{\mathrm{I}}}{K_{\mathrm{II}}}-\mathrm{sign}(K_{\mathrm{II}})\sqrt{\left(\frac{K_{\mathrm{I}}}{K_{\mathrm{II}}}\right)^{2}+8}\right), \tag{63}$$

$$K_{\theta_{\mathrm{c}}}=\cos\frac{\theta_{\mathrm{c}}}{2}\left(K_{\mathrm{I}}\cos^{2}\frac{\theta_{\mathrm{c}}}{2}-\frac{3}{2}K_{\mathrm{II}}\sin\theta_{\mathrm{c}}\right)=K_{IC}, \tag{64}$$

which can determine the direction of fracture propagation and whether the fracture will propagate.

In this paper, the displacement extrapolation method is adopted to calculate SIFs, which can be expressed as:

$$\begin{aligned}K_{\mathrm{I}}&=2Gw\sqrt{\frac{2\pi}{r}}(\kappa+1),\\ K_{\mathrm{II}}&=2Gv\sqrt{\frac{2\pi}{r}}(\kappa+1),\end{aligned} \tag{65}$$

where w and v are the "aperture" and "ride", respectively, as visualized in Figure 2(a).

6 Numerical examples

6.1 KGD hydraulic fracture model

In case of zero lag and zero leak-off, the propagation of a HF in an impermeable medium is governed by two competing dissipative mechanisms [62]: one is the flow process characterized by fluid viscosity and injection rate; the other is the fracture process characterized by rock toughness. For the viscosity dominated HF propagation, the toughness dissipation is negligible compared to the energy consumed to viscosity fluid flow, and for the toughness dominated HF propagation, the viscous dissipation is so small that can be negligible compared to the energy consumed in fracturing the rock.

The ability of the coupled method in simulating the viscosity dominated HF and toughness dominated HF is presented here by comparing the numerical results obtained with an available analytical solution for the plane strain KGD model.

The analytical solutions for the plane strain KGD model are dependent on the dimensionless toughness K_m, which is defined as:

$$K_{m}=\frac{K^{'}}{\left(E^{'3}\mu^{'}Q_{0}\right)^{1/4}}, \tag{66}$$

where Q_0 is injection rate, the material parameters E', K' and μ' are defined as follows:

$$E^{'}=\frac{E}{1-\nu^{2}},\quad K^{'}=\sqrt{\frac{32}{\pi}}K_{IC},\quad \mu^{'}=12\mu. \tag{67}$$

The HF propagation regime is dominated by toughness when K_m is larger than 4.0, and is dominated by viscosity when K_m is smaller than 1.0 [63].

The fractures are driven under a constant injection rate. The input parameters are listed in Table 1. Three different mesh densities are used, with element numbers of 1701, 6717 and 25037, respectively. The simulation results compared with the analytical solutions are presented below.

6.1.1 *Viscosity dominated fracture propagation*

To verify the viscosity dominated HF propagation regime, the fluid viscosity used here is μ=100 cP, and the evolution parameter K_m=0.92 is smaller than 1.0, which indicates that the simulated HF is in the viscosity dominated regime and thus can be approximated by the zero toughness solution. The simulation results and corresponding analytical solutions for the KGD models with the viscosity dominated HF propagation are shown in Figure 4. We can see that the numerical solution agrees well with the analytical solution.

6.1.2 *Toughness dominated fracture propagation*

To verify the viscosity dominated HF propagation regime, the fluid viscosity used here is μ=100 cP. The evolution parameter K_m=9.16 is larger than 4.0 throughout the fracture propagation, which indicates that the simulated HF is in the toughness dominated regime and thus can be approximated by the zero viscosity solution. The simulation results and corresponding analytical solutions for the KGD models with the toughness dominated HF propagation are shown in Figure 5. We can see that the numerical solution agrees well with the analytical solution except for the inlet pressure at the initial time. This is because an initial length of fracture should be given, which is used to start the calculation of the fluid flow. Therefore, there is a certain difference between the numerical solution and analytical solution at the initial time, this difference will be reduced with the mesh refinement and time evolution.

6.2 Permeability effect on the hydraulic fracture

In this section, the influence of the rock permeability on the

Table 1 Input parameters for KGD model

Parameter	Value
E (MPa)	17000
v	0.2
K_{IC} (MPa$\sqrt{\mathrm{m}}$)	1.46
Q_0 (m^2/s)	0.0001

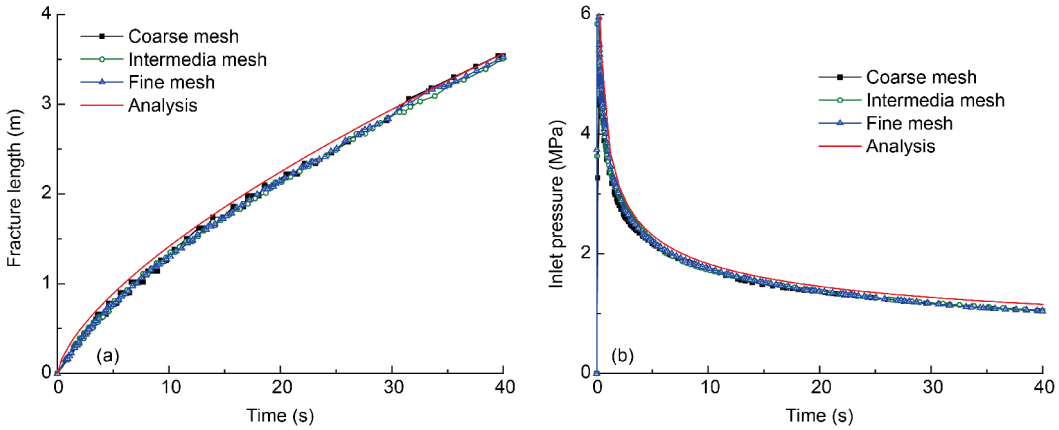

Figure 4 (Color online) Comparison of the results with analytical solution for the plane strain KGD model with viscosity dominated HF propagation. (a) Fracture opening at injection point; (b) inlet pressure at injection point.

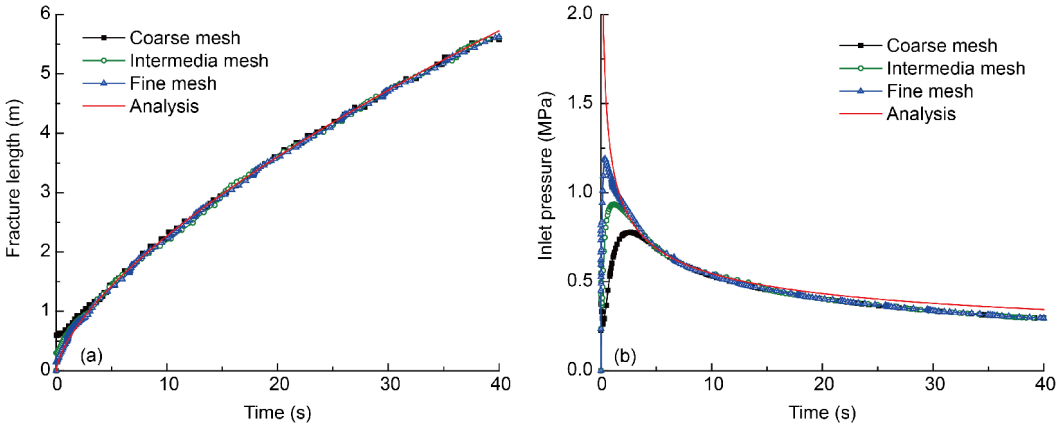

Figure 5 (Color online) Comparison of the results with analytical solution for the plane strain KGD model with toughness dominated HF propagation. (a) Fracture opening at injection point, (b) inlet pressure at injection point.

fracking process is studied. We consider the boundary value problem of a square domain with a given initial fracture of length a=8 m in its center, which is shown in Figure 6(a). The length and width of the domain are 80 m. The deformation at all sides is fixed and all the sides are assumed to be permeable, i.e. p=0.0 Pa. The material parameters are listed in Table 2. The evolution of a typical inlet fluid pressure curve over time is shown in Figure 6(b).

Figure 7(a)-(c) shows a fracture propagating in horizontal direction with the contour of fluid pressure at three different times. We can observe that the fluid pressure is higher within the fracture and adjacent zone, and nearly zero in the rest domain, because Poiseuille-type fluid inside the fracture flows rapidly compared to the Darcy's flow inside porous media. The fracture opening width along the fracture is shown in Figure 7(d). The pressure distribution inside the fracture is plotted for the different time in Figure 7(e). We can find that the pressure increases up to the point where the fracture begins to propagate. This is followed by a decreasing pressure due to the increasing fracture length and opening width, i.e. the fracture volume. The drop of pressure is well known in fracking, for example, the KGD solution in the previous subsection. During the further process, the fluid pressure again increases due to the influence of the fixed sides of the domain, which is different from the KGD solution because the KGD model is an infinite domain model, and the boundary is free.

Next, we consider the influence of the rock permeability on the fracking process. Figure 8(a)-(c) shows the fracture line and the contour of fluid pressure under different permeability of the media at time t=5 s. It can be found that the fracture does not propagate under a given injection rate if the permeability is large enough, as shown in Figure 8(a). If the permeability is small enough, the fluid is almost entirely inside the fracture, as shown in Figure 8(c). Further, the fracture can propagate for a period of time if the permeability is appropri-ate, as shown in Figure 8(b). Then it is arrested because the infiltrating area becomes large enough, the fluid leak-off rate and the injection rate achieve a balance.

6.3 Fluid flow in fracture network

In this section, the complex fluid field in the propagating fracture network is studied, which is the most advantage of this coupling method. The influence of the injection rate and the

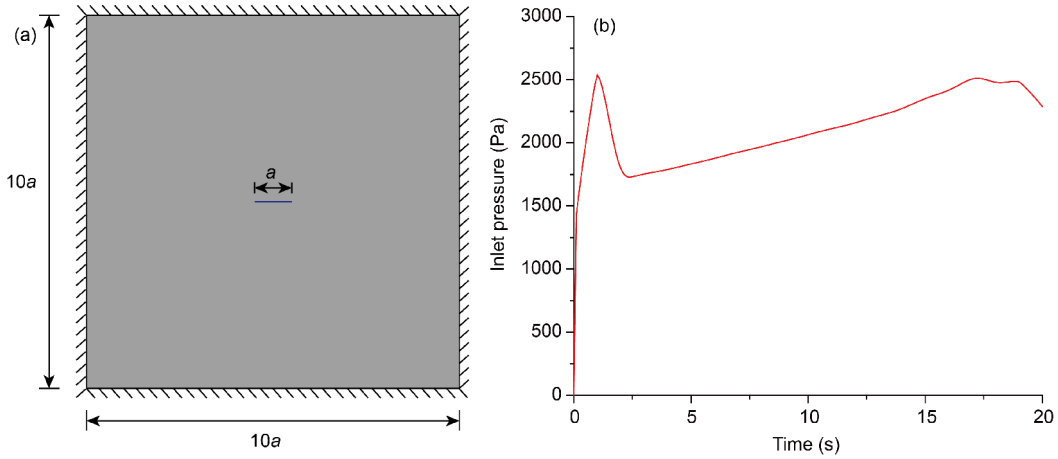

Figure 6 (Color online) Hydraulically induced fracture driven by fluid injection. (a) Boundary value problem. All the sides are mechanically constrained and are assumed to be permeable (p=0 Pa); (b) inlet fluid pressure p in the fracture over total injected time.

Table 2 Material parameters

Parameter	Value
E (MPa)	255
v	0.3
K_{IC} (MPa$\sqrt{\text{m}}$)	0.0167
Q_0 (m^2/s)	0.0004
α	1.0
v_u	0.358
μ (cP)	1.0
k (md) (1 md=9.87×10^{-14} m^2)	200

in-situ stress on the fracture network propagation is investigated in order to provide the guidance of fracture network optimization.

In this example, we consider a local HF network, which is one cluster of the whole network of HF in the current stage. An initial vertical main fracture and five horizontal NFs at the same interval are placed. The geometry and the boundary conditions are illustrated in Figure 9(b). The length and width of the domain are 10 m. The length of the main fracture and five NFs are 6 and 1.25 m, respectively. The material properties are the same as those listed in Table 2. The symmetry

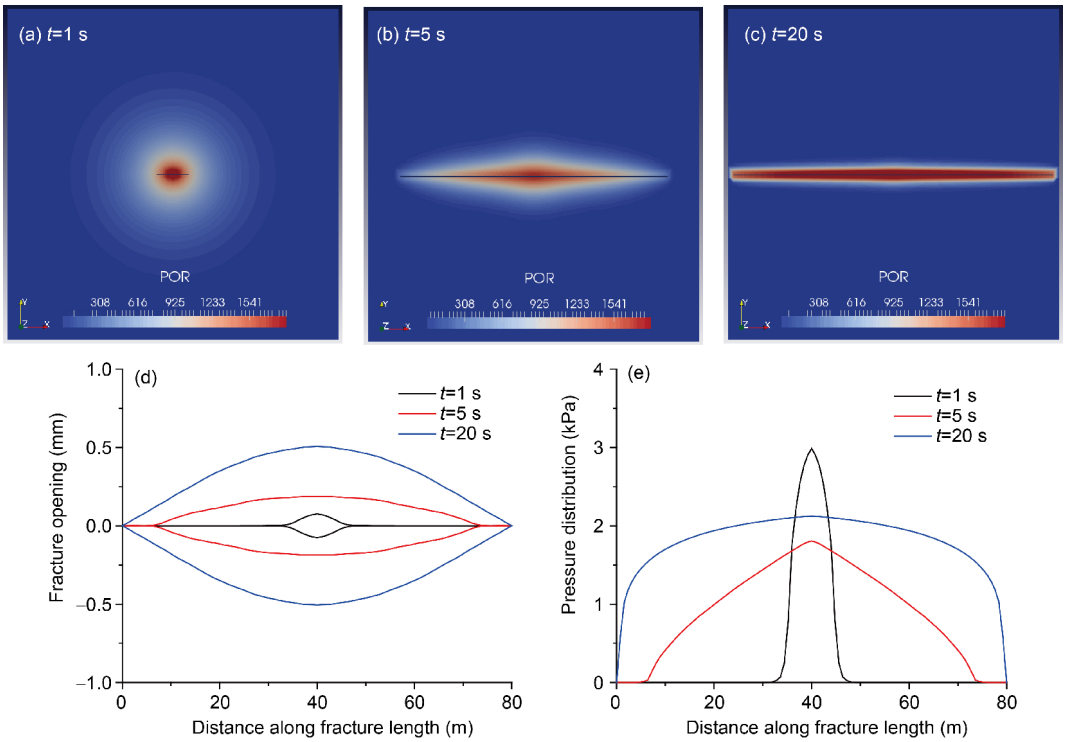

Figure 7 (Color online) Hydraulically induced fracture driven by fluid injection. (a)-(c) Fracture and fluid pressure p; fracture opening width w (d) and fluid pressure (e) along fracture at three times t=1, 5, 20 s, respectively.

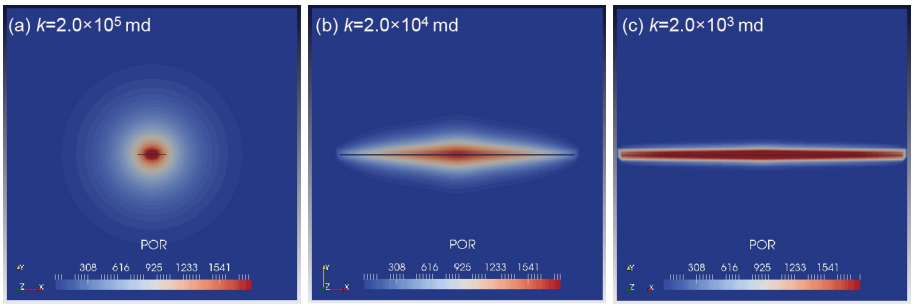

Figure 8 (Color online) Hydraulically induced fracture driven by fluid injection under different media permeability at time t=5 s. (a)-(c) The permeability of media is 2.0×10^5, 2.0×10^4 and 2.0×10^3 md, respectively.

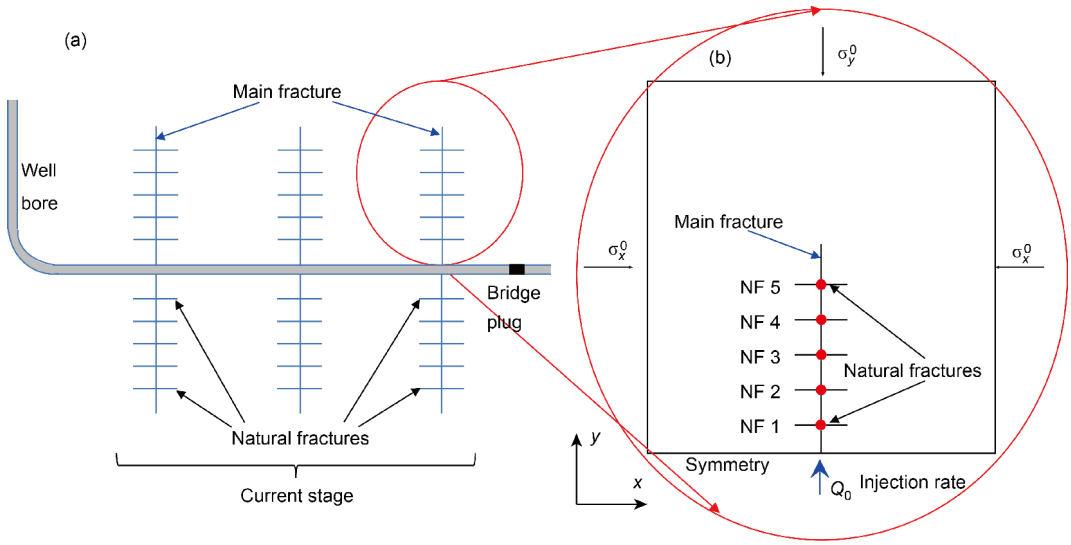

Figure 9 (Color online) (a) Hydraulically fracture network driven by fluid injection at current stage, a bridge plug is set to hydraulically isolate the previously stimulated stages; (b) local fracture network domain consists of HF and NFs for studying, lower side of the domain is the symmetry boundary and the other three sides are mechanically constrained and assumed to be permeable.

boundary is applied at the lower side of domain and the other three sides are mechanically constrained and assumed to be permeable. The fluid is injected from the inlet of the main fracture and then distributes into five NFs and drives them to propagate. Initially, the fractures are supported by the contact traction to prevent the penetration [64].

The injection rate Q_0 at the inlet of main fracture is $0.0002\,m^2/s$. The variations of the fluid pressure p at the inlet positions of five NFs (denoted by five red points in Figure 9(b)) with time are shown in Figure 10. It can be found that with the time evolution, the inlet pressure increases to a high value and then descends. The nearer the NF is to the main inlet, the higher the pressure is. Figure 11 shows the fracture evolution morphology at different time. After fracking, the fracture network is expanded and will be used for the gas output. It can be found that the NF near the injection point propagates further since more fluid flows into it.

Next the different injection rates are used to study the influence of injection rate on fracture network development. Figure 12 shows the fracture network morphology at time t=100 s corresponding to different injection rates. Corresponding to the largest injection rate, the fractures in Figure 12(c) fully propagate, and the fracture network is more uniform, which is considered more productive for the

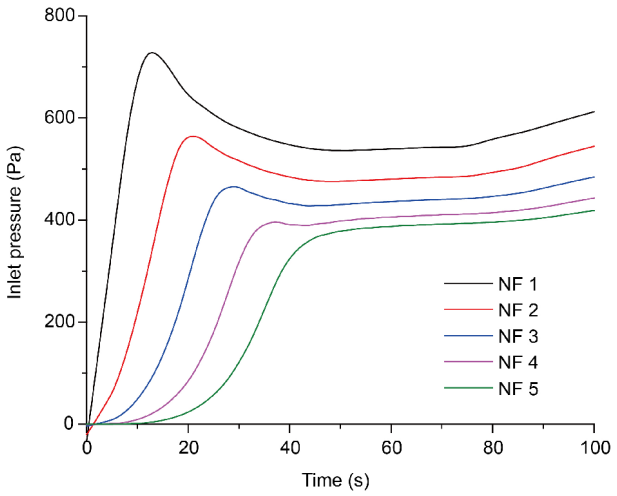

Figure 10 (Color online) Inlet fluid pressure of the five NFs over the total injected time.

gas and oil transport. The propagation length of the main fracture and five NFs under different injection rates are given in Figure 13. Interestingly, it is found that increasing the injection rate has a more significant influence on the development of horizontal NF than on the main fracture.

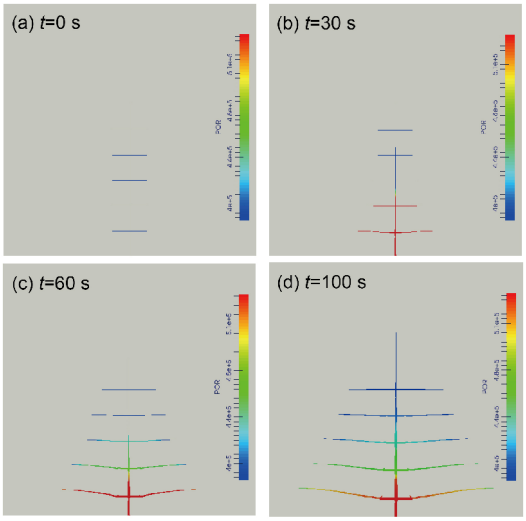

Figure 11 (Color online) Fracture evolution morphology for fracture network at different times. (a) t=0 s, (b) t=30 s, (c) t=60 s, (d) t=100 s, respectively.

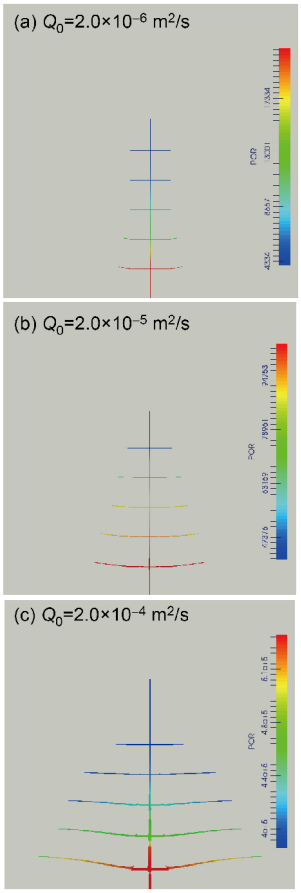

Figure 12 (Color online) Fracture network evolution morphology at the same time t=100 s with different inlet fluid flow rates. (a) Q_0=0.000002 m^2/s, (b) Q_0=0.00002 m^2/s, (c) Q_0=0.0002 m^2/s, respectively.

Further, the formation conditions, especially the *in-situ* stresses and initial pore pressure, also have great influence on forming complex fracture network. For a single HF, the fracture always tends to propagate in the direction of the maximum *in-situ* stress. However, it is more complex for the fracture network. Figure 14 shows the fracture network morphology and the fluid pressure contour under different *in-situ* stresses at time t=100 s. We can find that the fluid distribution is more uniform in Figure 14(d) (in this case, the *in-situ* stress in x-direction is the same as that in y-direction), and all the fractures (including one main fracture and five NFs) propagate simultaneously to generate a more uniform fracture network. The length of the main fracture and the total fracture network at different *in-situ* stress difference are given in Figure 15(a). It further demonstrates that small *in-situ* stress difference is good for the uniform development of fracture network. The final lengths of five NFs for different cases are all shown in Figure 15(b) and they nearly have an exponential decrease.

7 Concluding remarks

The main conclusions of this work are summarized below: (1) A new computational HF model is developed to study the fracking in permeable rocks. In this model, the fluid flow in fractures and rock media is solved in a unified framework by considering the fracture as a special porous media and introducing Poiseuille-type fluid flow inside the fracture. (2) The XFEM formulation for multiple fractures and fracture intersection in porous solid and finite element formulation for the

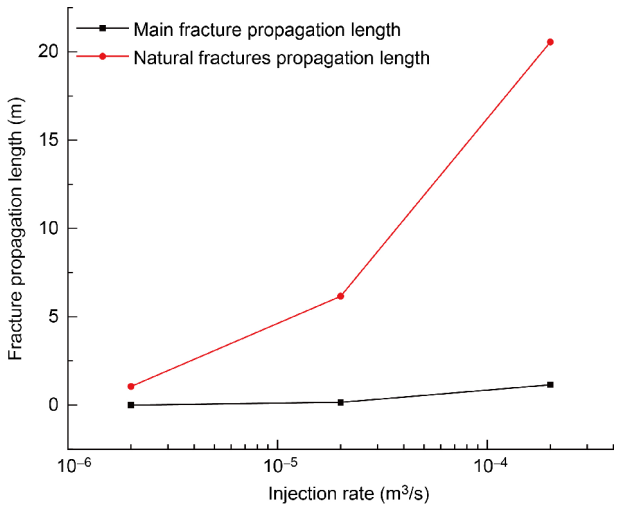

Figure 13 (Color online) The propagation length of one main fracture and five NFs under different injection rate.

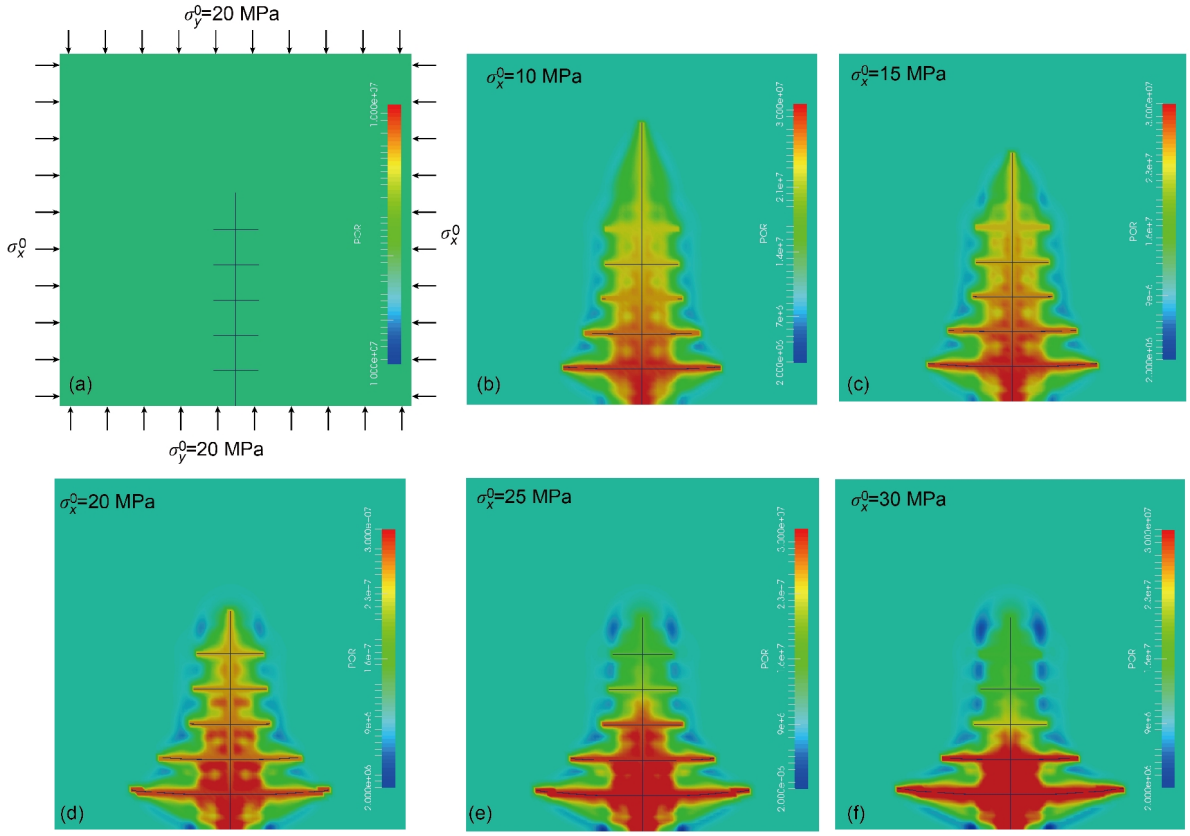

Figure 14 (Color online) Fracture evolution morphology for fracture network and the fluid pressure contour under different formation conditions. (a) The initial condition and *in-situ* stress configuration; (b)-(f) the simulation results for different *in-situ* stresses along *x*-direction at the same time *t*=100 s.

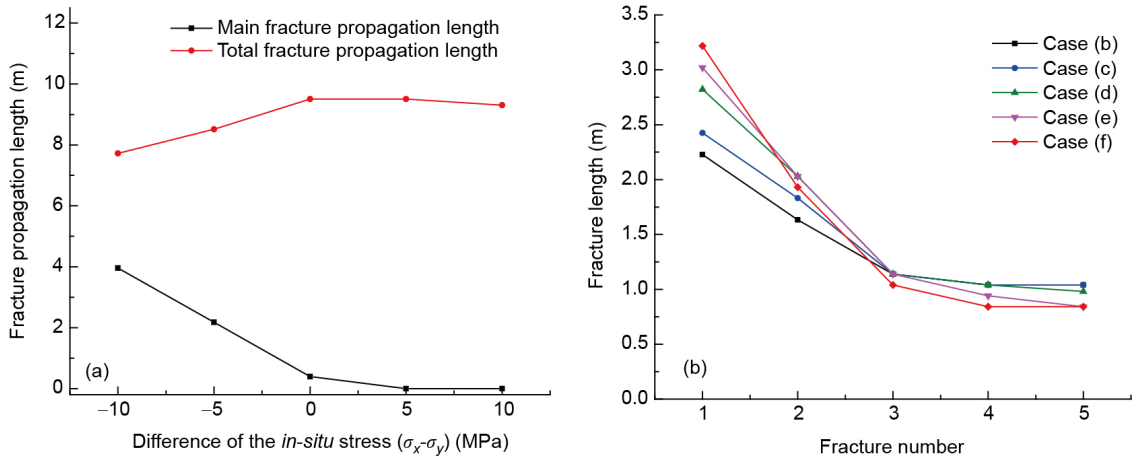

Figure 15 (Color online) (a) The vertical fracture propagation length and total fracture propagation length (one main fracture and five NFs) vs difference of *in-situ* stress; (b) the final length of five NFs (each point represents the fracture tip position of NF) corresponding to five cases in Figure 14(b)-(f).

unified fluid flow are derived based on virtual work principle. The most advantage of this coupling computation model is that it's convenient to deal with fluid flow inside the fracture network and in the rock. (3) The plane strain KGD model dominated by viscosity and toughness and the fluid flow inside the fracture network are simulated to show the accuracy and applicability of the coupling method. (4) Large injection rate, low rock permeability and isotropic *in-situ* stresses tend to lead to a more uniform and productive fracture network.

The findings in this study can help to understand some observed behaviors in the field of fracking and provide the guidance for fracture network optimization. For unconventional reservoirs, there is mainly soft rock with quasi-brittle fracture and strong anisotropy. It also contains many bedding planes and natural fractures. In order to simulate hydraulic fracturing in unconventional reservoirs, the future research should aim to develop a complete solution that takes into account the anisotropy of material constitutive and damage evolution

to model microscopic fractures in the present method.

This work was supported by the National Natural Science Foundation of China (Grant Nos. 11532008, and 11372157).

1 Z. P. Bažant, M. Salviato, V. T. Chau, H. Visnawathan, and A. Zubelewicz, J. Appl. Mech. **81**, 101010 (2014).
2 T. K. Perkins, and L. R. Kern, J. Pet. Tech. **13**, 937 (1961).
3 J. Geertsma, and F. De Klerk, J. Pet. Tech. **21**, 1571 (1969).
4 A. Settari, and M. P. Cleary, SPE Prod. Eng. **1**, 449 (1986).
5 R. de Borst, Mech. Res. Commun. **80**, 47 (2017).
6 C. Y. Dong, and C. J. de Pater, Comp. Methods Appl. Mech. Eng. **191**, 745 (2001).
7 M. J. Hunsweck, Y. Shen, and A. J. Lew, Int. J. Numer. Anal. Meth. Geomech. **37**, 993 (2013).
8 Z. Chen, A. P. Bunger, X. Zhang, and R. G. Jeffrey, Acta Mech. Solid Sin. **22**, 443 (2009).
9 M.W. McClure, and R.N. Horne, *Discrete Fracture Network Modeling of Hydraulic Stimulation: Coupling Flow and Geomechanics* (Springer Briefs in Earth Sciences, New York, 2013), p. 17.
10 C. Miehe, S. Mauthe, and S. Teichtmeister, J. Mech. Phys. Solids **82**, 186 (2015).
11 B. Lecampion, Commun. Numer. Meth. Engng. **25**, 121 (2009).
12 D. D. Xu, Z. L. Liu, and Z. Zhuang, Sci. China-Phys. Mech. Astron. **59**, 124631 (2016).
13 Z. Q. Yue, H. T. Xiao, L. G. Tham, C. F. Lee, and E. Pan, Comput. Mech. **36**, 459 (2005).
14 N. Moës, and T. Belytschko, Eng. Fract. Mech. **69**, 813 (2002).
15 Z. Chen, J. Pet. Sci. Eng. **88-89**, 136 (2012).
16 T. J. Boone, and A. R. Ingraffea, Int. J. Numer. Anal. Methods Geomech. **14**, 27 (1990).
17 T. Mohammadnejad, and A. R. Khoei, Finite Elem. Anal. Des. **73**, 77 (2013).
18 B. Carrier, and S. Granet, Eng. Fract. Mech. **79**, 312 (2012).
19 S. Salehi, and R. Nygaard, J. Energ. Resour. Technol. **137**, 012903 (2015).
20 Z. A. Wilson, and C. M. Landis, J. Mech. Phys. Solids **96**, 264 (2016).
21 K. Terzaghi, *Erdbaumechanik auf Bodenphysikalischer Grundlage* (Deuticke, Wien, 1925), p. 47.
22 M. A. Biot, J. Appl. Phys. **12**, 155 (1941).
23 O. Coussy, *Mechanics of Porous Continua* (John Wiley & Sons, Hoboken, 1995), p. 15.
24 E. Detournay, and H. D. C. Alexander, *Fundamentals of Poroelasticity* (Pergamon Press, C. Fairhurst, 1993), p. 113.
25 W. Ehlers, *Foundations of Multiphasic and Porous Materials* (Springer Berlin Heidelberg, Heidelberg, 2002), p. 3.
26 Q. Zeng, Z. Liu, D. Xu, H. Wang, and Z. Zhuang, Int. J. Numer. Meth. Eng. **106**, 1018 (2016).
27 D. Xu, Z. Liu, X. Liu, Q. Zeng, and Z. Zhuang, Comput. Mech. **54**, 489 (2014).
28 Z. Zhuang, Z. L. Liu, B. B. Cheng, and J. H. Liao, *Extended Finite Element Method* (Elsevier/Tsinghua University Press, Beijing, 2014), p. 189.
29 Q. L. Zeng, Z. L. Liu, D. D. Xu, and Z. Zhuang, Sci. China Technol. Sci. **57**, 1276 (2014).
30 M. Faivre, B. Paul, F. Golfier, R. Giot, P. Massin, and D. Colombo, Eng. Fract. Mech. **159**, 115 (2016).
31 S. Salimzadeh, and N. Khalili, Comp. Geotech. **69**, 82 (2015).
32 E. Gordeliy, and A. Peirce, Comp. Methods Appl. Mech. Eng. **283**, 474 (2015).
33 T. Mohammadnejad, and A. R. Khoei, Int. J. Numer. Anal. Meth. Geomech. **37**, 1247 (2013).
34 E. Gordeliy, and A. Peirce, Comp. Methods Appl. Mech. Eng. **253**, 305 (2013).
35 H. Ziegler, *Some Extremum Principles in Irreversible Thermodynamics, with Application to Continuum Mechanics* (Swiss Federal Institute of Technology, Zürich, 1962), p. 50.
36 M. A. Biot, and D. C. Drucker, J. Appl. Mech. **32**, 957 (1965).
37 P. M. Adler, J. F. Thovert, and V. V. Mourzenko, *Fractured Porous Media* (Oxford University Press, Oxford, 2012), p. 50.
38 J. Adachi, E. Siebrits, A. Peirce, and J. Desroches, Int. J. Rock Mech. Min. Sci. **44**, 739 (2007).
39 P. Gupta, and C. A. Duarte, Int. J. Numer. Anal. Meth. Geomech. **40**, 1402 (2016).
40 J. Réthoré, R. de Borst, and M. A. Abellan, Comput. Mech. **42**, 227 (2008).
41 A. R. Khoei, M. Vahab, and M. Hirmand, Int. J. Fract. **197**, 1 (2016).
42 A. R. Khoei, M. Hirmand, M. Vahab, and M. Bazargan, Int. J. Numer. Meth. Eng. **104**, 439 (2015).
43 M. Faivre, R. Giot, F. Golfier, and P. Massin, Rock Mech. Rock Eng. **1**, 1409 (2014).
44 Q. W. Ren, Y. W. Dong, and T. T. Yu, Sci. China Ser. E-Technol. Sci. **52**, 559 (2009).
45 D. D. Xu, Z. L. Liu, Z. Zhuang, Q. L. Zeng, and T. Wang, Sci. China-Phys. Mech. Astron. **60**, 024611 (2017).
46 J. Bear, *Dynamics of Fluids in Porous Media* (Courier Corporation, New York, 1972), p. 58.
47 M. K. Hubbert, *The Theory of Groundwater Motion* (Columbia University Press, Chicago, 1940), p. 785.
48 J. H. Song, P. M. A. Areias, and T. Belytschko, Int. J. Numer. Meth. Eng. **67**, 868 (2006).
49 A. Hansbo, and P. Hansbo, Comp. Methods Appl. Mech. Eng. **193**, 3523 (2004).
50 O. C. Zienkiewicz, Appl. Math. Mech. **3**, 457 (1982).
51 T. Belytschko, W. K. Liu, B. Moran, and K. Elkhodary, *Nonlinear Finite Elements for Continua and Structures* (John Wiley & Sons, New Jersey, 2013), p. 649.
52 T. Belytschko, H. Chen, J. Xu, and G. Zi, Int. J. Numer. Meth. Eng. **58**, 1873 (2003).
53 S. Natarajan, D. R. Mahapatra, and S. P. A. Bordas, Int. J. Numer. Meth. Eng. **31**, 269 (2010).
54 D. Wan, D. Hu, S. Natarajan, S. P. A. Bordas, and G. Yang, Int. J. Numer. Meth. Engng **110**, 203 (2017).
55 S. P. A. Bordas, T. Rabczuk, N. X. Hung, V. P. Nguyen, S. Natarajan, T. Bog, D. M. Quan, and N. V. Hiep, Comp. Struct. **88**, 1419 (2010).
56 D. P. Flanagan, and T. Belytschko, Int. J. Numer. Meth. Eng. **17**, 679 (1981).
57 W. J. T. Daniel, and T. Belytschko, Int. J. Numer. Meth. Eng. **64**, 335 (2005).
58 J. Chang, J. Xu, and Y. Mutoh, Eng. Fract. Mech. **73**, 1249 (2006).
59 F. Erdogan, and G. C. Sih, J. Basic Eng. **85**, 519 (1963).
60 J. L. Beuth Jr., and C. T. Herakovich, Theor. Appl. Fract. Mech. **11**, 27 (1989).
61 C. Carloni, and L. Nobile, Fat. Frac. Eng. Mat. Struct. **28**, 825 (2005).
62 E. Detournay, Int. J. Geomech. **4**, 35 (2004).
63 J. Hu, and D. I. Garagash, J. Eng. Mech. **136**, 1152 (2010).
64 A. R. Khoei, O. R. Barani, and M. Mofid, Int. J. Numer. Anal. Meth. Geomech. **35**, 1160 (2011).